THE JOURNAL OF PHYSICAL CHEMISTRY C

Subscriber access provided by UNIVERSITY OF TOLEDO LIBRARIES

C: Energy Conversion and Storage; Energy and Charge Transport

Magnetic Electrodeposition of Hierarchical Cobalt Oxide Nanostructure from Spent Lithium-Ion Batteries: Its Application as Supercapacitor Electrode

Eslam A.A. Aboelazm, Gomaa A.M. Ali, Hamed Algarni, Huajie Yin, Yu Lin Zhong, and Kwok Feng Chong

J. Phys. Chem. C, **Just Accepted Manuscript** • DOI: 10.1021/acs.jpcc.8b03306 • Publication Date (Web): 21 May 2018

Magnetic Electrodeposition of Hierarchical Cobalt Oxide Nanostructure from Spent Lithium-Ion Batteries: Its Application as Supercapacitor Electrode

Eslam A. A. Aboelazm [‡], *Gomaa A. M. Ali* [‡,§], *H. Algarni* [∥,⊥], *Huajie Yin* [†], *Yu Lin Zhong* [†], *Kwok Feng Chong* [‡,*]

[‡] Faculty of Industrial Sciences & Technology, Universiti Malaysia Pahang, Gambang, 26300 Kuantan, Malaysia

[§] Chemistry Department, Faculty of Science, Al–Azhar University, Assiut, 71524, Egypt

[∥] Research Centre for Advanced Materials Science (RCAMS), King Khalid University, Abha 61413, P. O. Box 9004, Saudi Arabia

[⊥] Department of Physics, Faculty of Sciences, King Khalid University, P. O. Box 9004, Abha, Saudi Arabia

[†] Centre for Clean Environment and Energy, Gold Coast Campus, Griffith University, Queensland 4222, Australia

ABSTRACT: In this study, electrodeposition of cobalt oxide (Co_3O_4) from spent lithium-ion batteries is successfully enhanced by the magnetic field effect. In the presence of magnetic field, well-defined hierarchical Co_3O_4 nanostructures with higher electroactive surface area is formed during electrodeposition process. Electrochemical analysis shows that the enhanced Co_3O_4 nanostructures exhibit excellent charge storage capabilities of 1273 F g^{-1} at 1 A g^{-1}, approximately 4 times higher than the electrodeposited Co_3O_4 that is formed without magnetic field effect. It also reveals the high cycling stability of enhanced Co_3O_4 nanostructures, with 96% capacitance retention at 5000 charge discharge cycles. The results manifest the enhancement of Co_3O_4 recovery from spent lithium-ion batteries, which can be the potential electrode material for supercapacitors application.

INTRODUCTION

Cobalt oxide (Co_3O_4) has been widely investigated as the electrode material for supercapacitors due to its high conductivity and multiple oxidation states which lead to high redox activity for pseudocapacitance.[1-3] More importantly, it was reported to possess extremely high theoretical specific capacitance of up 3560 F g^{-1},[4] that attracts intense scientific interests. Nonetheless, its excellent potential as supercapacitors electrode must be balanced by the economical production of Co_3O_4. In 2018, cobalt metal from ores was traded at record-highest price of USD 80 kg^{-1}, motivating the search for sustainable source of cobalt metal. In this context, cobalt recovery from spent lithium-ion battery (LiB) is deemed as the economically feasible route. The main cathode material in a LiB commonly consists of $LiCoO_2$ powder and the cobalt content in a LiB is in the range of 5-20 wt%,[5] depending on the manufacturing process. Therefore, it is economically unwise to dispose the spent LiB without recovery of these precious metals.

The current technology of metal recovery from LiB can be divided into pyrometallurgical and hydrometallurgical processes. Pyrometallurgical process involves selective volatilization of scrapped battery at elevated temperature followed by condensation for metal recovery. It is commonly being used in battery recycling process due to its simplicity, however, at the cost of environment pollution as toxic gases are emitted. On the other hand, hydrometallurgical process offers an environmental benign approach to recover metal from spent battery, where electrodes from battery are dissolved in concentrated acids, followed by recovery through precipitation, extraction or electrodeposition.[6] Out of these, electrodeposition process has been proven as the viable process to recover cobalt as the conductive film on the electrode. The first report on the electrodeposition process to recover cobalt from spent lithium-ion batteries was reported by Freitas et al.[7] The nucleation mechanism during cobalt electrodeposition depends strongly on the solution composition, pH and applied potential etc., in which different structural morphology can be produced with different nucleation mechanisms, namely instantaneous or progressive growth.[8-12] The supercapacitive behavior of electrodeposited cobalt film recycled from LiB was reported by Garcia et al., to show specific capacitance of 601 F g^{-1}.[13] Though various studies had been also reported on the supercapacitive behavior of recovered cobalt from spent lithium-ion batteries,[14-15] none of them could achieve the capacitance values that are close to the theoretical capacitance value of Co_3O_4.

The current work is motivated by the ferromagnetic properties of cobalt, where magnetic field is applied during electrodeposition in order to achieve controlled morphology of the deposited film. It has been proven that the Lorentz force between magnetic field and electric field, could cause the magnetohydrodynamic phenomenon to enhance the electrodeposition process.[16-18] This force is strongly depending on the direction which it is dominated when the magnetic field perpendicular to the working electrode.[19] To the best of our knowledge, there

is no report on the capacitive study of electrodeposited cobalt under magnetic field. The current work reports on the structural and electrochemical studies of electrodeposited cobalt from spent LiB, under magnetic field.

EXPERIMENTAL SECTION

Leaching solution preparation. Fully discharged Samsung 3.7 V LiB was physically dismantled and separated. The cathode powder was washed with deionized water at 50 ^{o}C to remove the impurities, followed by drying at 80 °C for 24 h. The dried cathode powder (10 g) was dissolved in the leaching solution (470 mL of 3 M HCl and 30 mL of H_2O_2) and then stirred at 80 °C for 2 h (Equation 1). The leaching solution was adjusted to pH 5 using NaOH solution, used for the electrodeposition process.

$$LiCoO_{2(s)} + \frac{1}{2}H_2O_{2(l)} + 3HCl_{(aq)} \rightarrow CoCl_{2(aq)} + \frac{1}{2}O_{2(g)} + LiCl_{(aq)} + 2H_2O_{(aq)} \quad (1)$$

Magnetic electrodeposition. Three-electrode system was setup for the electrodeposition of cobalt from the leaching solution. Nickel foam as the working electrode was used as the substrate for electrodeposition, Pt wire was used as the counter electrode, Ag/AgCl was used as the reference electrode and a potentiostat (AUTOLAB PGSTAT 101) was used as the power supply. The electrodeposition process was performed by using chronoamperometry under constant voltage of -1.0 V for 20 s. A constant magnetic field of 4.41 T was applied perpendicular to the working electrode surface during the electrodeposition process,[20] by placing two arc magnets (MAGCRAFT) with opposite poles next to the electrochemical cell. The electrodeposited cobalt films are denoted as Co_3O_4 and Co_3O_4(MF), in the absence and presence of magnetic field, respectively. The deposited active materials on the nickel foam in case of Co_3O_4 and Co_3O_4(MF) were 0.6 and 1.2 mg, respectively.

Structural studies. The crystalline phase was investigated using a X–Ray Diffractometer (Rigaku Miniflex II), equipped with an automatic divergent slit. Diffraction patterns were obtained using Cu–Kα radiation (λ = 0.15418 nm) and a graphite monochromator. The sample morphology was investigated by a field emission scanning microscope (JEOL JSM–7800 F) operated at 30.0 kV and a high resolution transmission electron microscope (Philips Tecnai F20) operated at 200 keV.

Electrochemical studies. Electrochemical studies were performed in three-electrode system, by an AUTOLAB PGSTAT101 potentiostat/galvanostat with frequency response analyzer. Cyclic voltammetry (CV) and galvanostatic charge/discharge (CDC) tests were performed in the potential range between 0 and 0.4 V vs. Ag/AgCl (as a reference electrode) in 5 M KOH and Pt wire as a counter electrode. Electrochemical impedance spectroscopy (EIS) data were collected from 100 kHz to 10 mHz, at open circuit potential (OCP) with a.c. amplitude of 10 mV.

RESULTS AND DISCUSSION

Structural and morphological analyses. Figure 1 shows the X-ray diffraction patterns for electrodeposited Co_3O_4 and Co_3O_4(MF). It can be seen that the electrodeposited Co_3O_4 exhibits diffraction peaks at 19.4°, 38.25°, and 66.5°, which are corresponding to the (1 1 1), (3 1 1) and (4 4 0) planes of Co_3O_4 cubic structure (COD, 9005887). Under magnetic field effect, the (1 1 1) plane of Co_3O_4(MF) is absent and it is deduced that the Co_3O_4(MF) crystal (3 1 1) and (4 4 0) planes are in the energetically favourable directions of magnetization, therefore enhancing the crystal growth along these directions, as reported by other studies.[16, 21] The crystallite size of the samples was calculated by Scherrer Equation[22] and it is found that Co_3O_4(MF) and Co_3O_4 have small crystallite size of 3.2 and 1.6 nm, respectively.

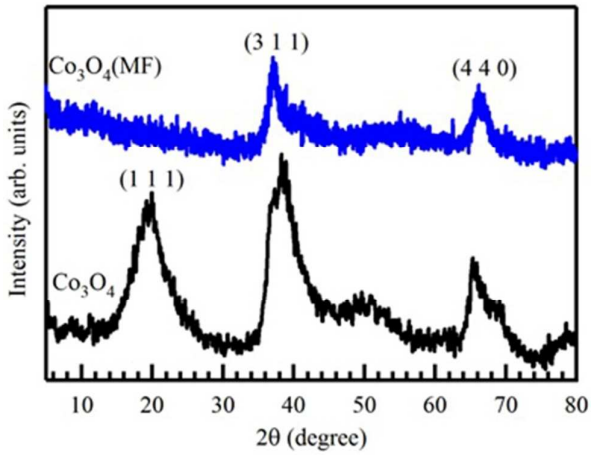

Figure 1. XRD patterns of Co_3O_4 and Co_3O_4(MF).

The missing (1 1 1) plane in Co_3O_4(MF) can also be observed from HRTEM image (Figure 2). The formation of Co_3O_4 in this work is in contrary with the previous studies that reported the formation of $Co(OH)_2$ during electrodeposition process.[7, 14, 23] We attribute such phenomenon to the electrochemical reduction of $Co(OH)_2$ (Equations 2 and 3) into metallic Co, followed by its oxidation into Co_3O_4 in the presence of oxidizing agent H_2O_2 in the electrolyte (Equation 4).[23] Short electrodeposition time (20 s) was applied in this work, forming thin layer of Co structure that oxidized rapidly into Co_3O_4 after the electrodeposition process stopped.

$$Co^{2+}_{(aq)} + 2OH^-_{(aq)} \rightarrow Co(OH)_{2\,(s)} \quad (2)$$

$$Co(OH)_{2(s)} + 2e^- \rightarrow Co_{\,(s)} + \, 2OH^-_{(aq)} \quad (3)$$

$$3Co_{(s)} + \, 4H_2O_{2_{(l)}} \rightarrow \, Co_3O_{4_{(s)}} \, + \, 4H_2O_{(l)} \quad (4)$$

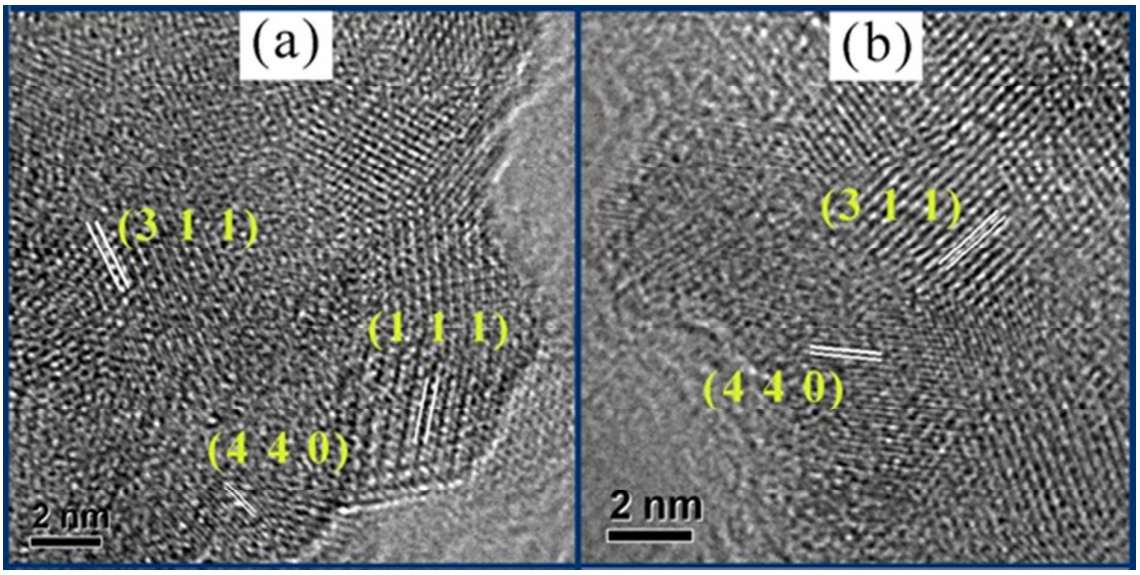

Figure 2. HRTEM of (a) Co_3O_4 and (b) Co_3O_4(MF).

The Co_3O_4 structures were further investigated by FESEM analyses as shown in Figure 3. Co_3O_4 exhibits agglomerated sheet-like structure, while Co_3O_4(MF) shows well-defined hierarchical nanosheets structure in which sheet thickness in the range of 25 - 28 nm (as shown in the inset). Such well-defined hierarchical structures of Co_3O_4(MF) facilitates ions diffusion within structure and allows maximum ions adsorption for charge storage purpose.[24] The Co_3O_4(MF) formation can be understood from the proposed mechanism as Figure S1. The electrodeposition begins with the nucleation of $Co(OH)_2$ particles, followed by the electrochemical reduction to form metallic cobalt that aggregates to form the sheet-like structure. As the electrodeposition is a random process, the sheet-like structure of cobalt agglomerates into uncontrolled morphology. In the presence of magnetic field, the aggregation of cobalt occurs in the controlled morphology due to the ferromagnetic properties of cobalt. Such uniaxial aggregation produces the hierarchical nanostructures and it is rapidly oxidized into Co_3O_4 in the presence of H_2O_2.

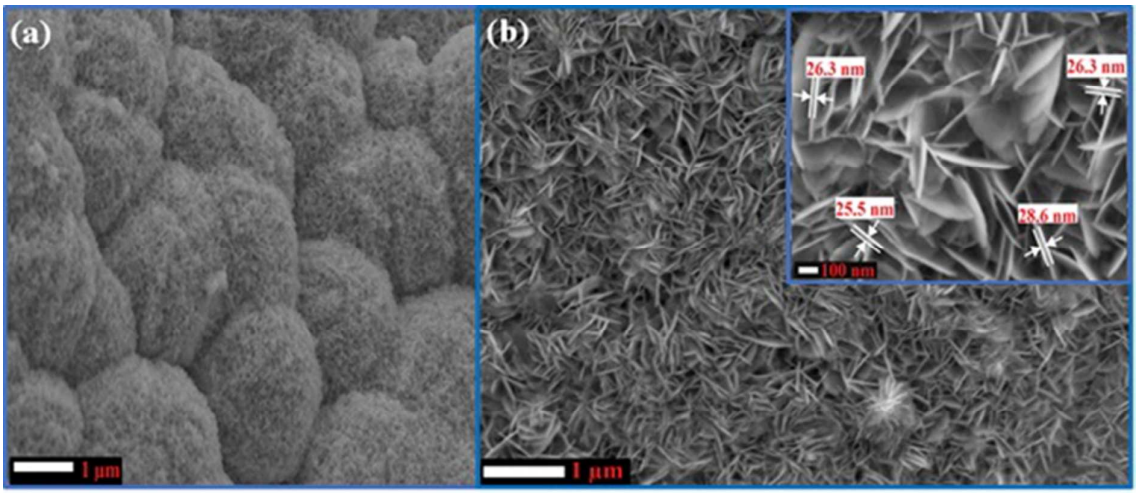

Figure 3. FESEM images of (a) Co_3O_4 and (b) Co_3O_4(MF), inset shows the Co_3O_4 sheets thickness.

Electrochemical studies. Figure 4(a) shows the cyclic voltammograms (CV) of Co_3O_4 and Co_3O_4(MF) electrodes. Both CV curves show two reversible redox peaks; first redox peak (O1/R1) at 0.27/0.19 V for Co_3O_4 and 0.2/0.12 V for Co_3O_4(MF), which can be correlated to redox reaction of Co^{2+}/Co^{3+} (Equation 5). Second peak (O2/R2) at 0.31/0.23 V for Co_3O_4 and 0.26/0.14 V for Co_3O_4(MF), which can be correlated to redox reaction of Co^{3+}/Co^{4+} (Equation 6).[25] It is worth noting that the CV curve of Co_3O_4(MF) electrode possesses significant higher area under the curve, as compared to that of Co_3O_4 electrode. This indicates that higher charge accumulated at Co_3O_4(MF) electrode surface during the potential cycling process.

$$Co_3O_4 + OH^- + H_2O \leftrightharpoons 3CoOOH + e^- \quad (5)$$

$$CoOOH + OH^- \leftrightharpoons CoO_2 + H_2O + e^- \quad (6)$$

The Co_3O_4(MF) was further investigated by CV at different scan rates as shown in Figure 4(b) with inset to show the obvious redox peaks at lower scan rate (3 mV s^{-1}). The CV curves show that redox current is increasing at higher scan rate, predominantly due to faster ions diffusion to the electrode surface.[26-27] The relationship between redox current and scan rate is

summarized as Figure 4(c) where linear relationship can be established between redox current and square root of scan rate. It implies that the redox reaction is dominated by OH^- diffusion process.

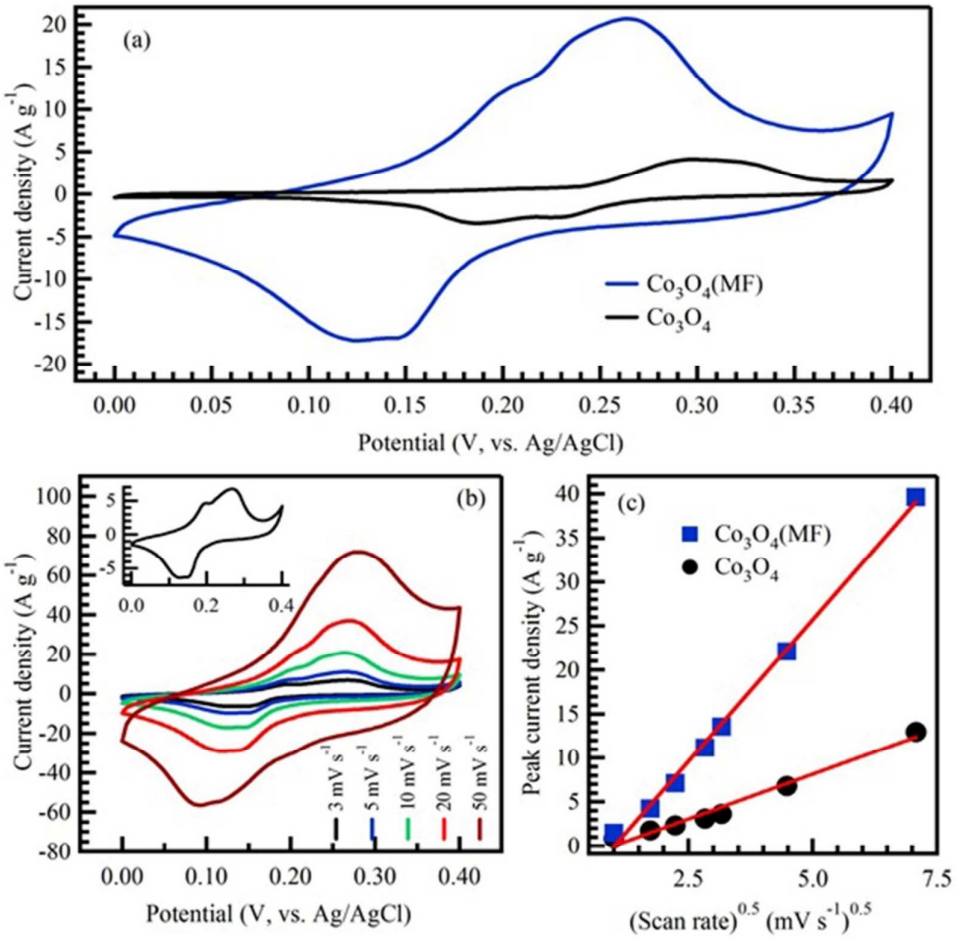

Figure 4. Cyclic voltammetry curves at (a) 10 mV s^{-1} of Co_3O_4 and Co_3O_4(MF), (b) different scan rates of Co_3O_4(MF): inset shows CV at 3 mV s^{-1}, and (c) peak current density versus square root of scan rate of Co_3O_4 and Co_3O_4(MF).

The diffusion coefficient (D) values of Co_3O_4 and Co_3O_4(MF) were calculated by Randles-Sevcik Equation as Equation (7).

$$i_P = 2.69 \times 10^5 \, n^{3/2} \, S_A \, D^{1/2} \, C \, v^{1/2} \quad (7)$$

where, i_p is the peak current (A), n is the number of electrons in the redox reaction, S_A is the electroactive surface area (cm^2), v is the scan rate ($V\ s^{-1}$) and C is the concentration of the electroactive species ($g\ cm^{-3}$) at the electrode. It can be seen that S_A plays an important role in the calculation of D values. Since the electrodes in this work were produced by electrodeposition process and it is impossible to accurately measure the S_A values, thus the ratio of S_A for Co_3O_4 and Co_3O_4(MF) were calculated by using the data obtained from EIS findings (Refer Supplementary Info for detailed S_A ratio calculation). According to the S_A ratio, the S_A for Co_3O_4(MF) is about 2.3 times higher than that for Co_3O_4. The S_A ratio was later used in the calculation of D ratio, by comparing the slope of curves in Figure 4(c) (Refer Supplementary Info for detailed D ratio calculation). It was found that the D value for Co_3O_4(MF) is about 8 times higher than that for Co_3O_4. Both enhanced S_A and D values for Co_3O_4(MF) electrodes can be associated to the well-defined hierarchical nanostructures of Co_3O_4(MF), which facilitates ions diffusion. Apart from that, the absence of (1 1 1) plane in Co_3O_4(MF) also indicates the dominance of other crystal planes, which will result in more cobalt atoms on the surface of Co_3O_4(MF) crystals as only 1.875 Co^{2+} are present in the (1 1 1) plane. This is also consistent with other study to report on the enhancement of the electrochemical performance of Co_3O_4 by suppression of (1 1 1) plane.[28]

The kinetics of charge storage in Co_3O_4 and Co_3O_4(MF) electrodes were studied by Trasatti's analysis. The total stored charge in an electrode can be divided into three fractions: the faradaic contribution from the slow ions insertion process limited by solid-state ion diffusion, the faradaic contribution from the fast charge-transfer process at surfaces or known as pseudocapacitance, and the nonfaradaic contribution from the fast electric double layer effect.[29] The former one is regarded as diffusive charge storage while the latter two are known as capacitive charge storage. In Trasatti's analysis, the charge storage processes can be represented by the following Equations:[30-32]

$$Q_{(\upsilon)} = Q_C + \alpha\upsilon^{-1/2} \quad (8)$$

$$1/Q_{(\upsilon)} = 1/Q_T + \alpha\upsilon^{1/2} \quad (9)$$

where $Q_{(\upsilon)}$ is the total measured voltammetric charge, Q_C is the capacitive charge (from both double layer and pseudocapacitive processes), Q_T is the total amount of stored charge, α is a constant and υ represents the scan rate. In Equation (8), the diffusive charge storage can be excluded as υ approaches infinite, therefore extrapolating the plot of $Q_{(\upsilon)}$ vs $\upsilon^{-1/2}$ (Figure 5(a)) gives the capacitive charge storage (Q_C) at intercept. In Equation (9), as the υ approaching 0, the electrochemical reaction time-scale is long enough to allow ions to access to all sites in electrode and the extrapolation of $1/Q_{(\upsilon)}$ vs $\upsilon^{1/2}$ (Figure 5(b)) allows the calculation of Q_T at intercept. The diffusive charge storage (Q_D) can be obtained from the difference between Q_T and Q_C. Table 1 summarizes the contribution of capacitive charge storage (Q_C) in Co_3O_4 and Co_3O_4(MF). It is worth mentioning that higher %Q_C (74.64%) can be found in Co_3O_4(MF) electrode. This can be explained by the higher S_A that contributes to higher double layer capacitance and faster ions diffusion and redox reaction that contribute to higher pseudocapacitance in Co_3O_4(MF).

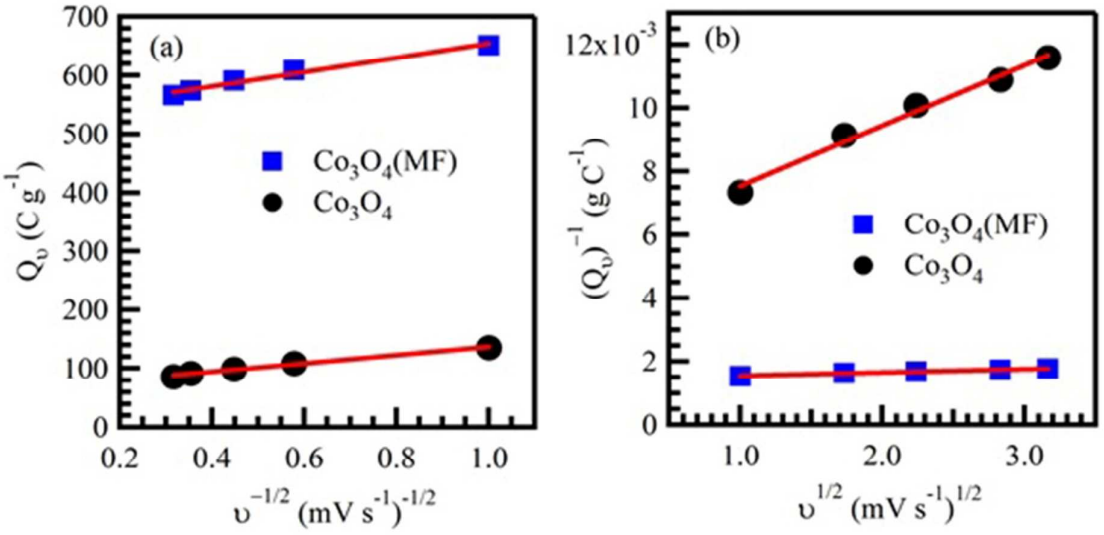

Figure 5. Dependence of (a) $Q_{(\upsilon)}$ on $\upsilon^{-1/2}$ and (b) $1/Q_{(\upsilon)}$ on $\upsilon^{1/2}$ for Co_3O_4 and Co_3O_4(MF).

Table 1. Total charge (Q_T), capacitive charge (Q_C), and capacitive charge contribution %Qc for Co_3O_4 and Co_3O_4(MF).

Material	Q_T (C g^{-1})	Q_C (C g^{-1})	%Q_C
Co_3O_4	178.57	66.27	37.11
Co_3O_4(MF)	714.28	533.16	74.64

The electrode performance was further investigated by galvanostatic charge/discharge (CDC) to simulate the practical supercapacitors application (Figure 6(a)). It can be seen that both Co_3O_4 and Co_3O_4(MF) electrodes exhibit linear (EDLC) CDC curves with two shoulders (pseudocapacitance). As CV findings, the pseudocapacitance of Co_3O_4 and Co_3O_4(MF) electrode arise from the redox reaction of Co^{2+}/Co^{3+} and Co^{3+}/Co^{4+}. Both Co_3O_4 and Co_3O_4(MF) do not exhibit significant iR drop at CDC curves, implying good electrode conductivity. However, it is pronounced that Co_3O_4(MF) electrode possesses longer discharge curve, as compared to that of Co_3O_4 electrode, indicating large specific capacitance of Co_3O_4(MF) electrode. The specific capacitance values were computed[33] and summarized in Figure 6(b). The highest specific capacitance of 1273 F g^{-1} is attained on Co_3O_4(MF) electrode at 1 A g^{-1}, approximately 4 times higher than that on Co_3O_4 electrode (315 F g^{-1}). Such enhancement is parallel to the CV findings where higher redox current can be found in Co_3O_4(MF) electrode. In addition, Co_3O_4(MF) electrode also demonstrates high rate capability by showing identical CDC curves at different current densities (Figure 6(c)). The obtained capacitance is compared with those reported values of cobalt oxide prepared by other methods as listed in Table 2.

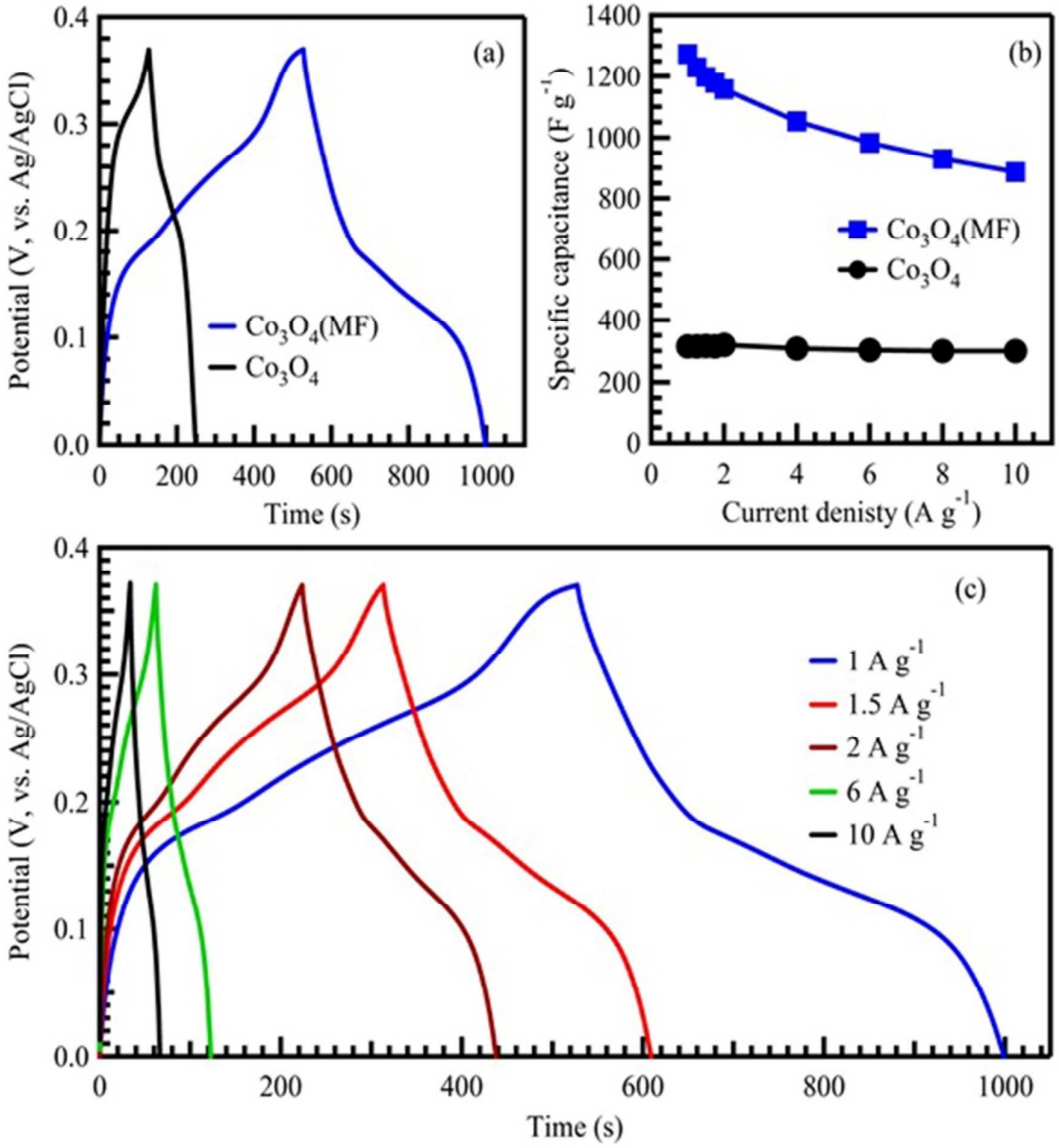

Figure 6. (a) Galvanostatic charge/discharge curves at 1 A g^{-1}, (b) specific capacitance as a function of current density for Co_3O_4 and Co_3O_4(MF) and (c) charge/discharge curves at different current densities of Co_3O_4(MF).

Table 2. Comparison of reported specific capacitance and stability with cobalt oxide prepared by other methods and precursors.

Method	Morphology	Specific capacitance (F g^{-1})		Stability (%)	Ref.
		CDC	CV		
Conventional reflux and microwave-assisted	Co_3O_4 nanowires	336.0 @ 1 A g^{-1}	355.0 @ 5 mV s^{-1}	99.1 @ 400 cycles	34
Hydrothermal	Nanoparticles of Co_3O_4/graphene	545.0 @ 0.5 A g^{-1}	----	82.4 @ 1000 cycles	34
	Nanocubes of Co_3O_4	----	430.6 @ 10 mV s^{-1}	85.0 @ 1000 cycles	35
Low temperature solution process	Nanoparticles of Co_3O_4	----	304.0 @ 5 mV s^{-1}	88.6 @ 1000 cycles	36
Citrate-gel	Co_3O_4 nanoparticles are embedded in SiO_2 matrix	679.0 @ 1 A g^{-1}	1143.0 @ 2.5 mV s^{-1}	92.0 @ 900 cycles	37
Electrophoretic deposition	Carbon nanotube/Co_3O_4 nanocomposites	705.0 @ 3 A g^{-1}	----	125.0 @ 10000 cycles	38
Modified sol-gel	Ultrafine Co_3O_4 nanocrystals	742.3 @ 0.5 A g^{-1}	----	86.2 @ 2000 cycles	39
Facile one-step hydrothermal strategy	Large-scale Co_3O_4 nanoparticles	928.0 @ 1.2 A g^{-1}		93.0 @ 2200 cycles	40

Electrochemical recycling	Amorphous particles of Co_3O_4	----	31.2 @ 1 mV s^{-1}	----	14
	Agglomerated crystals of Co_3O_4	----	13.0 @ 1 mV s^{-1}	----	15
Hydrothermal	3D flower like of CoS	409.3 @ 1 A g^{-1}	698.3 @ 5 mV s^{-1}	95.0 @ 1000 cycles	41
Electrochemical recycling	High porosity sheets like of $Co(OH)_2$	601.0 @ 0.23 mA cm^{-2}	625.0 @ 50 mV s^{-1}	----	4
Hydrothermal	Co_3O_4 cube-like	----	833.0 @ 50 mV s^{-1}	----	42
Heat treatment	Amorphous particles of $LiCoO_2$	730.0 @ 1 A g^{-1}	----	86.9 @ 4000 cycles	43
Magnetic electrodeposition	**Hierarchical nanostructure of Co_3O_4**	**1273.0 @ 1 A g^{-1}**	----	**96.0 @ 5000 cycles**	**This work**

The long-term potential cycling stability was tested over 5000 CDC cycles for both Co_3O_4 and Co_3O_4(MF) electrodes at high current density of 10 A g^{-1} as shown in Figure 7. Considering cobalt oxide as the pseudocapacitive material, potential cycling stability is often being compromised as the redox reaction could alter the electrode structure after long potential cycling process. Such common problem is observed at Co_3O_4 electrode where capacitance retention drops after 2000 CDC cycles and only achieves 81% of capacitance retention after 5000 CDC cycles. On Co_3O_4(MF) electrode, it is surprising that capacitance retention remains stable throughout the CDC cycles and high capacitance retention of 96% is achieved after 5000 CDC cycles. Representative CDC curves of the 1st, 2500th and 5000th cycles are shown in the inset of Figure 7. As compared in Table 2, Co_3O_4(MF) shows the highest stability with longer cycling. In addition, Co_3O_4(MF) electrode also exhibits high Coulombic efficiency of 97% (inset of Figure 7), which is higher than that reported for Co_3O_4-MnO_2-NiO ternary hybrid 1D nanotube arrays (92%).[44] We attribute this observation to the facile ions diffusion within the well-defined hierarchical nanostructures of Co_3O_4(MF), therefore minimizes the blockage to internal structure, as shown in Co_3O_4.

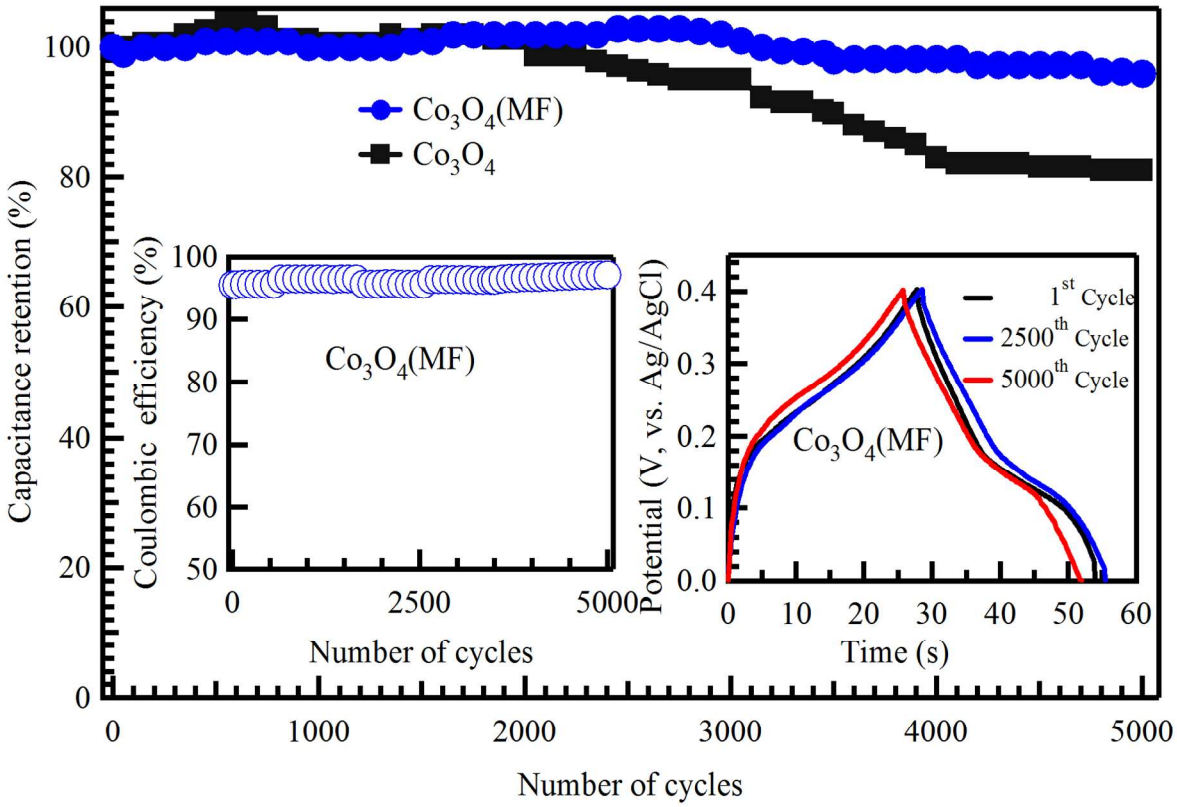

Figure 7. Cycling stability for Co_3O_4 and Co_3O_4(MF), inset show Coulombic efficiency and representative CDC cycles for Co_3O_4(MF).

Electrochemical impedance spectroscopy (EIS) was carried out to investigate the charge kinetic properties of the electrode in a frequency range from 0.1 Hz to 100 kHz at OCP. Figure 8(a) shows Nyquist plots of Co_3O_4 and Co_3O_4(MF) electrodes, with inset represents zoomed-in Nyquist plots at high-frequency region. The equivalent circuit is shown in Figure 8(b) as inset and all the fitting parameters are listed in Table S1. It shows that Co_3O_4(MF) possesses lower *ESR* (0.18 Ω) and R_{CT} (0.05 Ω), as compared to that of Co_3O_4 (*ESR* = 0.31 Ω; R_{CT} = 0.06 Ω). Low *ESR* in Co_3O_4(MF) renders its application as high power supercapacitor as the power delivery is inversely proportional to the *ESR*. This is a result of the well-defined hierarchical

nanosheets structure and high surface area of Co_3O_4(MF) which enhance the transportation of redox species within the structure.[45] Bode plot in Figure 8(b) describes the relationship between phase angle and frequency which shows both Co_3O_4 and Co_3O_4(MF) electrodes exhibit a good capacitive performance (84.2° and 75.4°, respectively) as the ideal capacitor phase angle is at 90°.[46] The relaxation time (τ) was calculated using the following Equation:

$$\tau = \frac{1}{f_o} \quad (10)$$

while (f_o) is frequency at the phase angle of 45° and they were computed to be 0.47 and 0.20 s for Co_3O_4 and Co_3O_4(MF) electrodes, respectively. Shorter relaxation time indicates that Co_3O_4(MF) electrode could switch more rapidly from resistive behavior to capacitive behavior. The real and the imaginary parts of capacitance were calculated and plotted as shown in Fig. 8(c) and (d) using the following Equations:

$$C'(\omega) = \frac{-Z''(\omega)}{\omega\,|Z(\omega)|^2 m} \quad (11)$$

$$C''(\omega) = \frac{Z'(\omega)}{\omega\,|Z(\omega)|^2 m} \quad (12)$$

where C' and C'' are the capacitance real and imaginary parts and $\omega = 2\pi f$, in order to study the dependence of specific capacitance on frequency. The total capacity of the sample is the sum of its C' and C'' and it can be seen that Co_3O_4(MF) electrode exhibits higher capacitance than Co_3O_4 electrode at all frequency range, which is in agreement with CDC findings.

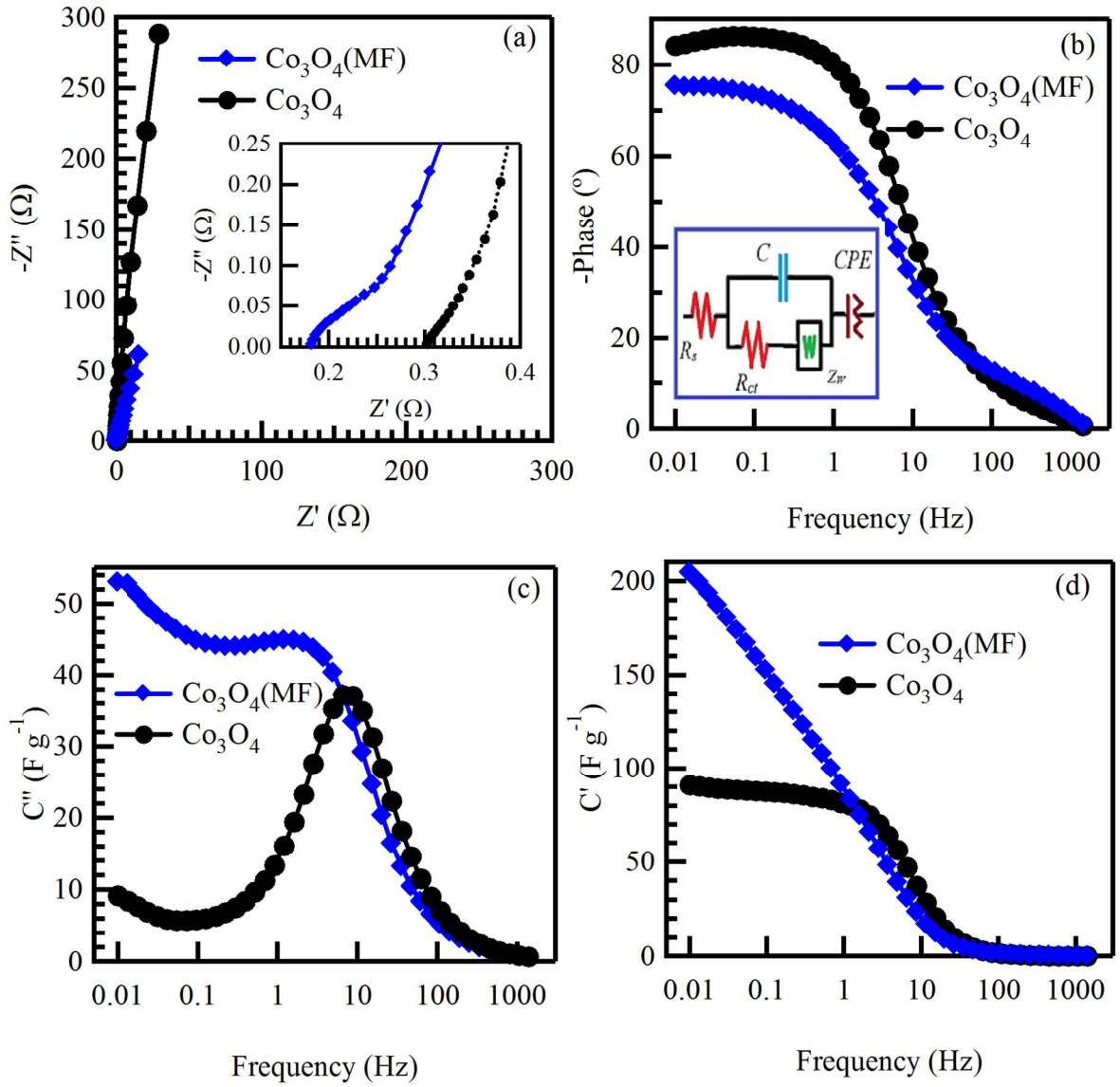

Figure 8. (a) Nyquist plots: the inset is zoomed view at high-frequency region, (b) Bode plots with equivalent circuit as inset, (c) real and (d) imaginary parts of the capacitance as functions of the frequency of Co_3O_4 and Co_3O_4(MF).

CONCLUSIONS

The effect of magnetic field on the electrodeposition of cobalt oxide from lithium-ion battery was studied. XRD and HRTEM show the absence of a crystal plane after applying the magnetic

field as it is energetically not favorable directions of magnetization. The results reveal a change in the surface morphology from agglomerated sheet-like structure to controlled morphology of well-defined hierarchical nanostructure. Moreover, both diffusion coefficient (*D*) and electroactive surface area are increased in Co_3O_4(MF) as a result of the morphology enhancement. Co_3O_4(MF) shows higher electrochemical performance in terms of specific capacitance (1273 F g^{-1}) which is 4 times higher than Co_3O_4 electrode which (315 F g^{-1}) as well as higher capacitive charge storage (Q_C). Besides the cyclic stability is found to be 96% after 5000 cycles. Finally, the impedance results also show lower equivalent series resistance (*ESR*), and charge transfer resistance (R_{CT}) of Co_3O_4(MF) than as compared to that of Co_3O_4.

ACKNOWLEDGMENTS

This work was supported by Ministry of Education Malaysia FRGS [RDU160118: FRGS/1/2016/STG07/UMP/02/3] and Universiti Malaysia Pahang [grant number RDU170357]. Moreover, the authors extend their appreciation to the Deanship of Scientific Research at King Khalid University for funding this work through research groups program under grant number (R.G.P.2/2/38).

AUTHOR INFORMATION

Corresponding Author Fax: +609 5492766. E-mail: ckfeng@ump.edu.my

Notes The authors declare no competing financial interest.

ASSOCIATED CONTENT

Supporting Information Detailed materials characterization results (EDX mapping, BET, CV, and other electrochemical data). This material is available free of charge via the Internet at http://pubs.acs.org/.

REFERENCES

1. Tian, X.; Sun, X.; Jiang, Z.; Jiang, Z.-J.; Hao, X.; Shao, D.; Maiyalagan, T., Exploration of the active center structure of nitrogen-doped graphene for control over the growth of Co_3O_4 for a high-performance supercapacitor. *ACS Appl. Energy Mater.* **2018**, *1*, 143-153.

2. Pal, M.; Rakshit, R.; Singh, A. K.; Mandal, K., Ultra high supercapacitance of ultra small Co_3O_4 nanocubes. *Energy* **2016**, *103*, 481-486.

3. Liu, X.; Shi, C.; Zhai, C.; Cheng, M.; Liu, Q.; Wang, G., Cobalt-based layered metal–organic framework as an ultrahigh capacity supercapacitor electrode material. *ACS Appl. Mater. Interfaces* **2016**, *8*, 4585-4591.

4. Cheng, G.; Kou, T.; Zhang, J.; Si, C.; Gao, H.; Zhang, Z., O_2^{2-}/O^- functionalized oxygen-deficient Co_3O_4 nanorods as high performance supercapacitor electrodes and electrocatalysts towards water splitting. *Nano Energy* **2017**, *38*, 155-166.

5. Guan, J.; Li, Y.; Guo, Y.; Su, R.; Gao, G.; Song, H.; Yuan, H.; Liang, B.; Guo, Z., Mechanochemical process enhanced cobalt and lithium recycling from wasted lithium-ion batteries. *ACS Sustainable Chem. Eng.* **2017**, *5*, 1026-1032.

6. Ordoñez, J.; Gago, E. J.; Girard, A., Processes and technologies for the recycling and recovery of spent lithium-ion batteries. *Renewable and Sustainable Energy Rev.* **2016**, *60*, 195-205.

7. Freitas, M. B. J. G.; Garcia, E. M., Electrochemical recycling of cobalt from cathodes of spent lithium-ion batteries. *J. Power Sources* **2007**, *171*, 953-959.

8. Schiavi, P. G.; Altimari, P.; Zanoni, R.; Pagnanelli, F., Morphology-controlled synthesis of cobalt nanostructures by facile electrodeposition: transition from hexagonal nanoplatelets to nanoflakes. *Electrochim. Acta* **2016**, *220*, 405-416.

9. Pagnanelli, F.; Altimari, P.; Bellagamba, M.; Granata, G.; Moscardini, E.; Schiavi, P. G.; Toro, L., Pulsed electrodeposition of cobalt nanoparticles on copper: influence of the operating parameters on size distribution and morphology. *Electrochim. Acta* **2015**, *155*, 228-235.

10. Brasiliense, V.; Clausmeyer, J.; Dauphin, A. L.; Noël, J.-M.; Berto, P.; Tessier, G.; Schuhmann, W.; Kanoufi, F., Opto-electrochemical in situ monitoring of the cathodic formation of single cobalt nanoparticles. *Angew. Chem. Int. Ed.* **2017**, *56*, 10598-10601.

11. Li, M.; Gao, B.; Shi, Z.; Hu, X.; Wang, S.; Li, L.; Wang, Z.; Yu, J., Electrodeposition of cobalt from urea-acetamide-LiBr melt. *J. Solid State Electrochem.* **2016**, *20*, 247-254.

12. Sniekers, J.; Geysens, P.; Malaquías, J. C.; Vander Hoogerstraete, T.; Van Meervelt, L.; Fransaer, J.; Binnemans, K., Cobalt (II) containing liquid metal salts for electrodeposition of cobalt and electrochemical nanoparticle formation. *Dalton Trans.* **2017**, *46*, 12845-12855.

13. Garcia, E. M.; Tarôco, H. A.; Matencio, T.; Domingues, R. Z.; dos Santos, J. A. F.; Ferreira, R. V.; Lorençon, E.; Lima, D. Q.; Freitas, M. B. J. G., Electrochemical recycling of

cobalt from spent cathodes of lithium-ion batteries: its application as supercapacitor. *J. Appl. Electrochem.* **2012**, *42*, 361-366.

14. Barbieri, E. M. S.; Lima, E. P. C.; Cantarino, S. J.; Lelis, M. F. F.; Freitas, M. B. J. G., Recycling of spent ion-lithium batteries as cobalt hydroxide, and cobalt oxide films formed under a conductive glass substrate, and their electrochemical properties. *J. Power Sources* **2014**, *269*, 158-163.

15. Barbieri, E. M. S.; Lima, E. P. C.; Lelis, M. F. F.; Freitas, M. B. J. G., Recycling of cobalt from spent Li-ion batteries as β-$Co(OH)_2$ and the application of Co_3O_4 as a pseudocapacitor. *J. Power Sources* **2014**, *270*, 158-165.

16. Olvera, S.; Arce Estrada, E. M.; Sanchez-Marcos, J.; Palomares, F. J.; Vazquez, L.; Herrasti, P., Effect of the low magnetic field on the electrodeposition of Co_xNi_{100-x} alloys. *Mater. Charact.* **2015**, *105*, 136-143.

17. Yu, Y.; Song, Z.; Ge, H.; Wei, G.; Jiang, L., Effects of magnetic fields on the electrodeposition process of cobalt. *Int. J. Electrochem. Sci.* **2015**, *10*, 4812-4819.

18. Fattahi, A.; Bahrololoom, M. E., Investigating the effect of magnetic field on pulse electrodeposition of magnetic and non-magnetic nanostructured metals. *Surf. Coat. Technol.* **2015**, *261*, 426-435.

19. Thiemig, D.; Kubeil, C.; Gräf, C. P.; Bund, A., Electrocodeposition of magnetic nickel matrix nanocomposites in a static magnetic field. *Thin Solid Films* **2009**, *517*, 1636-1644.

20. Elias, L.; Hegde, A. C., Effect of magnetic field on corrosion protection efficacy of Ni-W alloy coatings. *J. Alloys Compd.* **2017**, *712*, 618-626.

21. Wu, C.; Wang, K.; Li, D.; Lou, C.; Zhao, Y.; Gao, Y.; Wang, Q., Tuning microstructure and magnetic properties of electrodeposited CoNiP films by high magnetic field annealing. *J. Magn. Magn. Mater.* **2016**, *416*, 61-65.

22. Patterson, A. L., The Scherrer formula for X-ray particle size determination. *Phys. Rev.* **1939**, *56*, 978-982.

23. Shaju, K.; Guerlou-Demourgues, L.; Godillot, G.; Weill, F.; Delmas, C., Strategies for synthesizing conductive spinel cobalt oxide nanoparticles for energy storage applications. *J. Electrochem. Soc.* **2012**, *159*, A1934-A1940.

24. Parveen, N.; Ansari, S. A.; Ansari, S. G.; Fouad, H.; Abd El-Salam, N. M.; Cho, M. H., Solid-state symmetrical supercapacitor based on hierarchical flower-like nickel sulfide with shape-controlled morphological evolution. *Electrochim. Acta* **2018**, *268*, 82-93.

25. Salunkhe, R. R.; Tang, J.; Kamachi, Y.; Nakato, T.; Kim, J. H.; Yamauchi, Y., Asymmetric supercapacitors using 3D nanoporous carbon and cobalt oxide electrodes synthesized from a single metal–organic framework. *ACS Nano* **2015**, *9*, 6288-6296.

26. Mai, L.; Li, H.; Zhao, Y.; Xu, L.; Xu, X.; Luo, Y.; Zhang, Z.; Ke, W.; Niu, C.; Zhang, Q., Fast ionic diffusion-enabled nanoflake electrode by spontaneous electrochemical pre-intercalation for high-performance supercapacitor. *Sci. Rep.* **2013**, *3*, 1718.

27. Ali, G. A. M.; Tan, L. L.; Jose, R.; Yusoff, M. M.; Chong, K. F., Electrochemical performance studies of MnO_2 nanoflowers recovered from spent battery. *Mater. Res. Bull.* **2014**, *60*, 5-9.

28. Liu, D.; Wang, X.; Wang, X.; Tian, W.; Bando, Y.; Golberg, D., Co_3O_4 nanocages with highly exposed {110} facets for high-performance lithium storage. *Sci. Rep.* **2013**, *3*, 2543-2549.

29. Brezesinski, T.; Wang, J.; Tolbert, S. H.; Dunn, B., Ordered mesoporous α-MoO_3 with iso-oriented nanocrystalline walls for thin-film pseudocapacitors. *Nat. Mater.* **2010**, *9*, 146-151.

30. Ardizzone, S.; Fregonara, G.; Trasatti, S., "Inner" and "outer" active surface of RuO_2 electrodes. *Electrochim. Acta* **1990**, *35*, 263-267.

31. Baronetto, D.; Krstajić, N.; Trasatti, S., Reply to "note on a method to interrelate inner and outer electrode areas" by H. Vogt. *Electrochim. Acta* **1994**, *39*, 2359-2362.

32. Ali, G. A. M.; Yusoff, M. M.; Algarni, H.; Chong, K. F., One-step electrosynthesis of MnO_2/rGO nanocomposite and its enhanced electrochemical performance. *Ceram. Int.* **2018**, *44*, 7799-7807.

33. Pachfule, P.; Shinde, D.; Majumder, M.; Xu, Q., Fabrication of carbon nanorods and graphene nanoribbons from a metal–organic framework. *Nat. Chem.* **2016**, *8*, 718-724.

34. Nguyen, T. T.; Deivasigamani, R. K.; Kharismadewi, D.; Iwai, Y.; Shim, J.-J., Facile synthesis of cobalt oxide/reduced graphene oxide composites for electrochemical capacitor and sensor applications. *Solid State Sci.* **2016**, *53*, 71-77.

35. Jang, G.-S.; Ameen, S.; Akhtar, M. S.; Shin, H.-S., Cobalt oxide nanocubes as electrode material for the performance evaluation of electrochemical supercapacitor. *Ceram. Int.* **2018**, *44*, 588-595.

36. Li, Z.-Y.; Bui, P. T.; Kwak, D.-H.; Akhtar, M. S.; Yang, O.-B., Enhanced electrochemical activity of low temperature solution process synthesized Co_3O_4 nanoparticles for pseudo-supercapacitors applications. *Ceram. Int.* **2016**, *42*, 1879-1885.

37. Ali, G. A. M.; Fouad, O. A.; Makhlouf, S. A.; Yusoff, M. M.; Chong, K. F., Co_3O_4/SiO_2 nanocomposites for supercapacitor application. *J. Solid State Electrochem.* **2014**, *18*, 2505-2512.

38. Kumar, N.; Yu, Y.-C.; Lu, Y. H.; Tseng, T. Y., Fabrication of carbon nanotube/cobalt oxide nanocomposites via electrophoretic deposition for supercapacitor electrodes. *J. Mater. Sci.* **2016**, *51*, 2320-2329.

39. Wang, X.; Sumboja, A.; Khoo, E.; Yan, C.; Lee, P. S., Cryogel synthesis of hierarchical interconnected macro-/mesoporous Co_3O_4 with superb electrochemical energy storage. *J. Phys. Chem. C* **2012**, *116*, 4930-4935.

40. Yuan, C.; Yang, L.; Hou, L.; Shen, L.; Zhang, F.; Li, D.; Zhang, X., Large-scale Co_3O_4 nanoparticles growing on nickel sheets via a one-step strategy and their ultra-highly reversible redox reaction toward supercapacitors. *J. Mater. Chem.* **2011**, *21*, 18183-18185.

41. Chen, H.; Zhu, X.; Chang, Y.; Cai, J.; Zhao, R., 3D flower-like CoS hierarchitectures recycled from spent $LiCoO_2$ batteries and its application in electrochemical capacitor. *Mater. Lett.* **2018**, *218*, 40-43.

42. Samal, R.; Dash, B.; Sarangi, C. K.; Sanjay, K.; Subbaiah, T.; Senanayake, G.; Minakshi, M., Influence of synthesis temperature on the growth and surface morphology of Co_3O_4 nanocubes for supercapacitor applications. *Nanomaterials* **2017**, *7*, 356-369.

43. Xu, Y.; Dong, Y.; Han, X.; Wang, X.; Wang, Y.; Jiao, L.; Yuan, H., Application for simply recovered $LiCoO_2$ material as a high-performance candidate for supercapacitor in aqueous system. *ACS Sustainable Chem. Eng.* **2015**, *3*, 2435-2442.

44. Singh, A. K.; Sarkar, D.; Karmakar, K.; Mandal, K.; Khan, G. G., High-performance supercapacitor electrode based on cobalt oxide–manganese dioxide–nickel oxide ternary 1D hybrid nanotubes. *ACS Appl. Mater. Interfaces* **2016**, *8*, 20786-20792.

45. Fan, H., et al., Thin Co_3O_4 nanosheet array on 3D porous graphene/nickel foam as a binder-free electrode for high-performance supercapacitors. *Electrochim. Acta* **2016**, *188*, 222-229.

46. Shao, Y.; Li, J.; Li, Y.; Wang, H.; Zhang, Q.; Kaner, R. B., Flexible quasi-solid-state planar micro-supercapacitor based on cellular graphene films. *Mater. Horiz.* **2017**, *4*, 1145-1150.

TOC Graphic

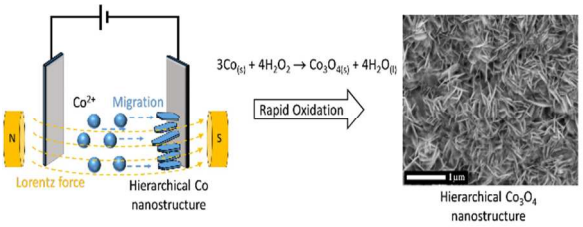
$3Co_{(s)} + 4H_2O_2 \rightarrow Co_3O_{4(s)} + 4H_2O_{(l)}$
Rapid Oxidation
Co^{2+}
Migration
N
S
Lorentz force
Hierarchical Co nanostructure
1μm
Hierarchical Co_3O_4 nanostructure